Journal of Materials Chemistry B

ROYAL SOCIETY OF CHEMISTRY

PAPER

View Article Online
View Journal | View Issue

Cite this: J. Mater. Chem. B, 2022, 10, 8502

3D bio-printing of photocrosslinked anatomically tooth-shaped scaffolds for alveolar ridge preservation after tooth extraction†

Haihuan Gong,[ab] Yanyan Zhao,[b] Qiwei Chen,[b] Yilin Wang,[b] Hong Zhao,[c] Jing Zhong,[b] Qing Lan,[a] Ying Jiang*[a] and Wenhua Huang*[abc]

Alveolar ridge preservation techniques have been developed as a possible method to maintain the optimum ridge contour and dimensions. Grafting a bone substitute is paramount to prevent alveolar ridge resorption after tooth extraction. However, it remains a great challenge to develop alveolar ridge preservation materials with sufficient mechanical strength, bioactivity, and osteoinductivity and favorable tooth extraction socket morphological matching. In this work, a novel photocrosslinked composite ink consisting of nacre, polyurethane (PU) and polyhedral oligomeric silsesquioxane (POSS) was prepared and used to fabricate 3D porous scaffolds for alveolar ridge preservation. This nacre/PU/POSS (NPP) composite was characterized in terms of its rheological behavior, mechanical properties, and surface hydrophilicity. The biomineralization of these NPP scaffolds was confirmed *via in vitro* experiments. MC3T3-E1 cells were distributed homogeneously on the NPP scaffolds and stimulated cellular proliferation. When the NPP scaffolds were grafted into the sockets after extraction of mandibular incisors, the height and width of alveolar bone resorption were reduced, and new bone formation was observed. These NPP composites are promising scaffold materials for alveolar ridge preservation and 3D printing of bone grafts in future.

Received 13th June 2022,
Accepted 15th September 2022

DOI: 10.1039/d2tb01229d

rsc.li/materials-b

1. Introduction

Surgical extraction may be clinically required when a tooth cannot be restored by prosthetic treatment.[1] A series of biological processes are initiated after tooth extraction, from the formation of blood clots and granulation tissue to the revascularization of vascularized to the bone substitution and reconstruction.[2,3] The main post-extraction consequences are the sustained absorption of the alveolar bone and the dramatic loss of the ridge volume (horizontally from 29% to 63% and vertically from 11% to 22%).[2,4,5] Alveolar bone volume reduction along with the ridge architecture morphological changes has considerable impacts on the functional and esthetic of tooth restoration treatment.[6,7] Thus, alveolar ridge preservation techniques have been developed to maintain the optimum ridge contour and dimensions.

Generally, autografts, allografts, and xenografts are used to fill the tooth socket immediately after tooth extraction to increase the bone volume.[5,8] Autologous bone grafts are the "gold standard" for bone regeneration,[1,9] but present some disadvantages, which are more painful and less acceptable to the patient, such as the requirement for a second surgery and the limited availability of bone supply.[10,11] Therefore, various synthetic bone substitutes have been developed.[12] Most of these commercial products are available as lyophilized powders and their physical properties make the socket preservation technique more sensitive.[13,14]

Meanwhile, it is difficult to maintain the socket steadily by using current granular shaped grafts. If better maintenance of the bone volume and contour is desired, biomaterials with a low degradation rate and mechanical stability should be chosen.[5,15–17] Considering the organic (20% type I collagen molecules)–inorganic (70% nanocrystals of hydroxyapatite) constituents of natural bone, an ideal bone scaffold needs a combination of a biocompatible polymer and inorganics.[18,19] Consequently, there is an increasing demand to develop high-performance biomaterials that match the mechanical properties

[a] Department of Stomatology, Affiliated Hospital of Guangdong Medical University, Zhanjiang, 524000, China. E-mail: huangwenhua2009@139.com, jy197701@163.com
[b] Guangdong Engineering Research Center for Translation of Medical 3D Printing Application, Guangdong Provincial Key Laboratory of Medical Biomechanics, Department of Human Anatomy, School of Basic Medical Sciences, Southern Medical University, Guangzhou, 510515, China
[c] Department of Human Anatomy, School of Basic Medical Sciences, Guangdong Medical University, Zhanjiang, 524000, China

† Electronic supplementary information (ESI) available. See DOI: https://doi.org/10.1039/d2tb01229d

of bone with excellent osteoconductivity to stimulate new bone regeneration.[18,20] In addition, it is also necessary to establish an extracellular matrix (ECM) to mimic the bone microenvironment and promote cell infiltration and proliferation for new bone formation. To achieve these objectives, three-dimensional (3D) printing has attracted much attention as an innovative alternative technology. It is one of the most promising techniques for fabricating materials with specific customized structures like native tissues, such as bone engineering scaffolds with controllable macroporous structures to allow efficient oxygen, nutrient, and metabolite exchange.[11,21,22]

While bone scaffolds have long relied almost exclusively on ceramics such as hydroxyapatite (HA), tricalcium phosphate (TCP) and their composites or on non-degradable metals, the extraction of bioactive agents of marine mollusc metabolites and/or shells has emerged as a promising alternative.[23,24] Indeed, nacre has demonstrated excellent biocompatibility, biodegradability, and osteoinductive properties for mineralization *in vitro*.[24–26] Previous research has shown that nacre can stimulate osteoblasts and is biocompatible with bone tissues when implanted in rats,[25,27] sheep,[28,29] and humans.[30] Considering that the water-soluble matrix (WSM) of nacre powder contains signal molecules, and its degradation rate is suitable (more readily dissolvable than calcium phosphate), adding nacre powder may be an efficient way to prepare scaffolds for alveolar ridge preservation with natural growth factors.[31]

Polyurethanes (PUs) have gained attention in biomedicine research owing to their excellent physical properties, biocompatibility, and bioactivity.[32–34] Degradable PU can be synthesized by selecting hydrolysis-prove polycaprolactone diol (PCL) based soft segments showed good biocompatibility. PU ensures an almost frictionless integration into the tissue and its viscoelastic properties are comparable with those of ceramics.[35] Moreover, PU can be modified by functionalizing the end of groups with hydroxyethyl methacrylate (HEMA) to form photopolymerizable PU,[36,37] for applications in repairing complexes and irregular bone defects. Polyhedral oligomeric silsesquioxane (POSS), the smallest hybrid silica nanoparticles, which is used to prepare new organic–inorganic hybrid materials, allows them to be incorporated effectively into the composite or the organic polymer matrix.[38,39] POSS cages can provide a larger surface area due to the nanosize structure (1–3 nm) compared with the microscale ceramic particles. Incorporating POSS into an polymer matrix can enhance the performance of the materials and significantly strengthen the interface.[40,41] However, the deficient osteoconductivity and osteoinductivity of these synthetic composites limit their further application in bone tissue repair and regeneration.

Herein, this study is aimed at developing a 3D interconnected porous scaffold with an in-organic–organic material to prevent or reduce the linear and volumetric changes in alveolar ridges in aesthetic areas after tooth extraction (Scheme 1). This novel 3D-printed composite scaffold combines the osteoinductive properties of nacre, the photocureability and printability of PU, and the excellent mechanical properties of POSS. In brief, photocureable PU was fabricated using PCL as the soft segments, and a range of nacre/PU/POSS (NPP) composites and 3D scaffolds were prepared. *In vitro* experiments were conducted systematically to characterize the scaffolds and determine their effects on cell behaviors, such as adhesion, proliferation, and differentiation. The performance of scaffolds for site preservation in post-extractive sockets was evaluated by micro-focal computed tomography (micro-CT) *in vivo*.

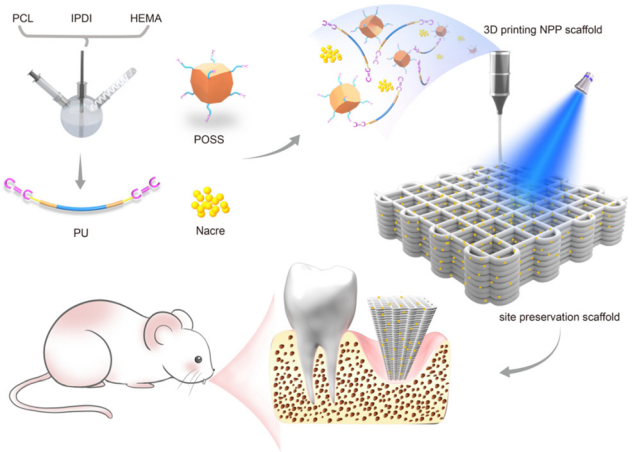

Scheme 1 Schematic illustration of the preparation of nacre/PU/POSS (NPP) scaffolds and their applications *in vivo*.

2. Experimental

2.1 Materials

Polycaprolactone diol (PCL, $\bar{M}_n$ = 2000 g mol^{-1}), isophorone diisocyanate (IPDI), 2-hydroxyethyl methacrylate (HEMA), dibutyltin dilaurate (DBTDL), and tetrahydrofuran (THF) were purchased from Sigma-Aldrich (USA). Nacre powder (the average particle size was 15 micron) was purchased from Jieshikang Biotechnology Co. Ltd (China). POSS (MA0735) was purchased from Hybrid Plastics, Inc. (USA). MC3T3-E1 Subclone 14 cells were provided by Cell Bank, Shanghai Institutes for Biological Sciences, Chinese Academy of Sciences. Fetal bovine serum (FBS) and α-minimum essential medium (α-MEM) were purchased from Gibco (Australia); streptomycin (100 mg ml^{-1}), penicillin (100 U ml^{-1}), Alamar Blue Cell Viability Assay Kit and Live/Dead assay kit were purchased from Thermo Fisher Scientific (USA). The alkaline phosphatase (ALP) kit was purchased from Beyotime (China) and the Alizarin red staining (ARS) kit was purchased from Cyagen (China).

2.2 Synthesis of photopolymerizable polyurethane (PU)

PCL was dried by azeotropic distillation with toluene before use, and THF and HEMA were dried sufficiently over 4 Å molecular sieves for 72 h. In three-neck round-bottom flasks with a mechanical stirrer and a water-cooled condenser, PU was synthesized at 68 °C under a nitrogen atmosphere, using a certain amount of THF as a solvent and DBTDL as a catalyst. NCO-terminated PU pre-polymers were first synthesized by chemical reactions that occur between PCL and IPDI for 3 h.

Afterwards, HEMA was added slowly to the pre-polymer and stirred. Heating was continued until the –OH group was no longer observed, while the C=C group was observed by Fourier transform infrared (FTIR) spectroscopy. The molar ratio of PCL : IPDI : HEMA was kept constant at 1 : 2 : 2.

2.3 Fabrication of nacre/PU/POSS (NPP) composites and scaffolds

Powdered nacre (10 g) was dissolved in ultra-pure water (20 ml) with continuous stirring for 20 h at room temperature and then centrifuged for 20 min at 3500 rpm. The supernatant was the water-soluble matrix (WSM) of nacre powders.[42] The NPP composites were prepared by stirring nacre, PU, POSS and photoinitiator LAP in the WSM at room temperature. Three groups of NPP composites were synthesized by varying the weight percentages of PU and POSS as follows:

NPP-0%: 50 wt% nacre + 50 wt% PU + 0 wt% POSS

NPP-5%: 50 wt% nacre + 45 wt% PU + 5 wt% POSS

NPP-10%: 50 wt% nacre + 40 wt% PU + 10 wt% POSS

(The amount of WSM added is 10% of the total mass in each group).

2.4 Characterization of NPP composites and scaffolds

2.4.1 Characterization of photopolymerizable PU. The NCO-terminated PU pre-polymers and C=C-terminated PU were characterized using a FTIR spectrometer (Thermo Nicolet iS5, USA) in the 650–4000 cm^{-1} recording range. ^1H NMR analyses were performed using a BRUKER AVANCE-III HD 500 MHZ spectrometer at room temperature.

2.4.2 Thermal characterization of NPP composites. The thermal stability of the synthesized NPP composites was assessed by thermogravimetry analysis (TGA; STA6000, USA), operating under a N_2 atmosphere at a heating rate of 10 °C min^{-1} from 30 °C to 600 °C. The glass transition temperatures of NPP composites were measured *via* differential scanning calorimetry (DSC; Q50, USA) from −60 to 100 °C at a rate of 10 °C min^{-1} under N_2.

2.4.3 Water contact angles. The surface hydrophilicity of the NPP composites was evaluated by measuring the static aqueous contact angles using a contact angle measurement (SL250, USA) instrument (n = 5).

2.4.4 AFM observation. The surface roughness of the NPP composites was measured by AFM (Bruker MultiMode 8, Germany) observation at the nano level. The image analysis was performed using the Nanoscope software.

2.4.5 Rheology and printability analysis. The viscoelastic properties of the NPP composites were measured using a rheometer (HAAKE MARS40, Germany) at 35 °C in a rotational test mode. The shear rate ranged from 0.1 to 1000 s^{-1}. The paste was extruded layer by layer at 25–40 °C from a programmed nozzle to form porous scaffolds with different shapes. The printing speed was set as 1.5–4.5 mm s^{-1}.

2.4.6 Mechanical properties. Compressive properties were assessed using a universal testing machine (UTM4204, China). Cuboid-shaped sample scaffolds were prepared with dimensions 10 × 10 × 5 mm using a 3D printing machine (3D-Bioplotter™, Germany) according to a predesigned 3D model. The macropore size was 500 μm, the printing speed was 3.0 mm s^{-1} and printing was performed with a needle of 22G (400 μm). All specimens were compressed at a speed of 5 mm min^{-1} at room temperature until they fail (n = 5).

2.5 Biomineralization *in vitro*

A field emission scanning electron microscope (SEM; Sigma500, Germany) equipped with an energy-dispersive spectrometry (EDS) system was used to analyze the surface morphology, elements, and contents of the NPP composite scaffolds after soaking in simulated body fluids (SBFs) for 7 days. The SBF volume ratio to the mass of the composite scaffold was 200 ml g^{-1}, similar to the previous report.[43]

2.6 Cell proliferation and live/dead assay

The biocompatibility of the NPP composite scaffolds was evaluated using MC3T3-E1 cells. The cells were cultured at 37 °C under a 5% CO_2 humidified atmosphere. The culture medium contains the 90% α-MEM culture medium, 10% fetal bovine serum, and 1% penicillin–streptomycin (PS). The medium was substituted every 2–3 days until the cell density reached 80–90% confluence, and the cells were digested with trypsin for subsequent use. All NPP scaffolds were sterilized by soaking in 75% (v/v) alcohol for 30 min and then irradiated for 2 h under UV light. The MC3T3-E1 cells were seeded on different scaffolds (50 μL of cell suspension) and placed in a 48-well culture plate. The cell viability was assessed using the Alamar Blue assay. In detail, Alamar Blue was added to each well in an amount at a concentration of 10% of the culture volume and incubated for 4 h. Then, 100 μL of supernatants were extracted and measured at wavelengths of 530–560 nm. Live/dead cells were stained after seeding on scaffolds and observed by inverted fluorescence microscopy (Olympus IX83, Tokyo, Japan). The results of days 1 and 3 were used to evaluate the cell viability and cell proliferation activity.

2.7 Cell osteogenic differentiation

MC3T3-E1 cells were seeded on each scaffold in a 48-well plate at a density of 5 × 10^3 cells per well and incubated in osteoinductive media (the α-MEM culture medium supplemented with 50 μg ml^{-1} ascorbic acid, 10 mM β-glycerophosphate, and 10 nM dexamethasone). The cells cultured in the osteogenic induction medium were used as a control, and the medium of all the groups was changed every 2–3 days. ALP staining was performed according to the instructions after the cells were seeded on scaffolds and cultured in the osteogenic induction medium for 7 days. The early osteogenesis-related marker ALP gene expressions were measured using the quantitative reverse transcription–polymerase chain reaction (qRT-PCR). Detailed experiments were performed on the basis of the standard protocol in previous studies.[44,45] The cells were collected after 7 days of culture on scaffolds. The primer sequences of the gene are listed in Table S1 (ESI†), and *GAPDH* as the housekeeping gene was used as the internal control. The experiments followed the $2^{-\Delta\Delta CT}$ method to quantify the relative expression of ALP.

Calcium deposition in the cells cultured on the NPP scaffolds for 14 days was evaluated using the Alizarin red staining (ARS) kit. Briefly, the cells on the surface of scaffolds were washed with PBS, fixed with 4% paraformaldehyde for 30 min, and stained in accordance with the procedure described in the kit.

2.8 Establishment and scaffold implantation of the tooth extraction model in rats

2.8.1 Rat tooth extraction model. Six-week-old-male Sprague Dawley (SD) rats with an average body weight of 160–200 g were purchased from the Laboratory Animal Center of Southern Medical University (Guangzhou, China), and all animal experiments were carried out in accordance with the Institutional Animal Ethics Committee of Southern Medical University. All rats were allowed to acclimatize for 7–10 days prior to the first procedure, and a classical rat tooth extraction socket site preservation model was established to evaluate the effect of NPP composite scaffolds. Briefly, the mandibular right incisor was ground off at the level of the gums with a dental drill bit every 3 days using ether anaesthesia (Fig. S3A, ESI†). On the 3rd day after three consecutive grindings, the gingiva around the right incisor was carefully separated with a dental probe, and the right incisor was carefully removed in a minimally invasive way after anesthesia (Sumianxin, 0.8 ml kg^{-1}). The rats were divided into three groups (n = 5) randomly, and various NPP scaffolds were implanted into the rat extraction socket. Sockets without scaffolds served as the control (Fig. S3B and C, ESI†). Finally, the gingival tissue was sutured using a 6-0 suture (Fig. S3D, ESI†). The rats were euthanized at designated time points (3 and 6 weeks) after the surgery. All rats were perfused with normal saline through the ascending aorta and with a 4% paraformaldehyde solution. The mandible was dissected and fixed in 4% paraformaldehyde before micro-CT analysis.

2.8.2 Micro-CT evaluation. Each mandible was scanned by micro-CT (ZKKS-MCT-Sharp, China) at a voltage of 70 kV, a current of 100 μA, and a slice thickness of 20 μm. The newly formed bone inside the extraction socket was the region of interest. 3D reconstruction analyses of the selected area were performed to directly observe the new alveolar bone tissue and evaluate the tooth socket bone healing. The bone mineral density (BMD) and bone volume fraction (bone volume/total volume, BV/TV) were calculated and statistically analyzed.

2.8.3 Measurement of alveolar bone resorption. The changes in the alveolar bone height and ridge width were measured according to the previous method[3,46] using the RadiAnt DICOM Viewer (Version 2021.2, Poland) software. The distances between the most superior point and the most inferior extent of the labial or lingual alveolar plate were measured on the non-extracted and extracted sides. To standardize the measurement results, the relative height and width were defined as the ratio of the extracted and unextracted distances for the same rat. The absorption rate (%) was calculated by the formula: $(1-(h1/h2))/100$, where "$h1$" denotes the height/width of the alveolar bone on the extracted side and "$h2$" denotes the height/width of the alveolar bone on the non-extracted side.

2.8.4 Histological analysis. After the micro-CT analysis, the bone specimens were decalcified in 10% EDTA for 2 months. The sample was then processed, dehydrated, embedded in paraffin, and cut into thin slices for hematoxylin and eosin (H&E) staining and Masson's trichrome staining. The stained images were captured under an inverted fluorescence microscope (Olympus IX83, Tokyo, Japan).

2.8.5 Toxicity *in vivo*. The major organs (heart, liver, spleen and kidneys) at week six were dissected using a scalpel and examined histologically to ensure the safety of the NPP scaffold material *in vivo*. The sample was fixed in 4% paraformaldehyde for 48 h, and the procedure of dehydration, embeddeding in paraffin, and cutting into thin slices for H&E staining was the same as that mentioned above. An optical microscope was used to observe the pathological changes in the tissues.

2.9 Statistical analysis

Each group included at least three samples ($n \geq 3$), and all data were presented as mean ± standard deviation. Because the values were normally distributed, the experimental data from all the studies were analyzed using a one-way analysis. When statistical differences were appeared, the LSD test and Dunnett T3 test were performed for *post hoc* multiple comparisons. The statistical significance was set at 5% (α = 0.05).

3. Results and discussion

3.1 Structural characterization of photopolymerizable PU

The synthesis of this photopolymerizable PU was based on a conventional solution polymerization process. As shown in Fig. 1A, the reaction of PCL polyol and IPDI produced an isocyanate (NCO)-terminated PU prepolymer; then, HEMA was added to react with the remaining NCO groups to form C═C

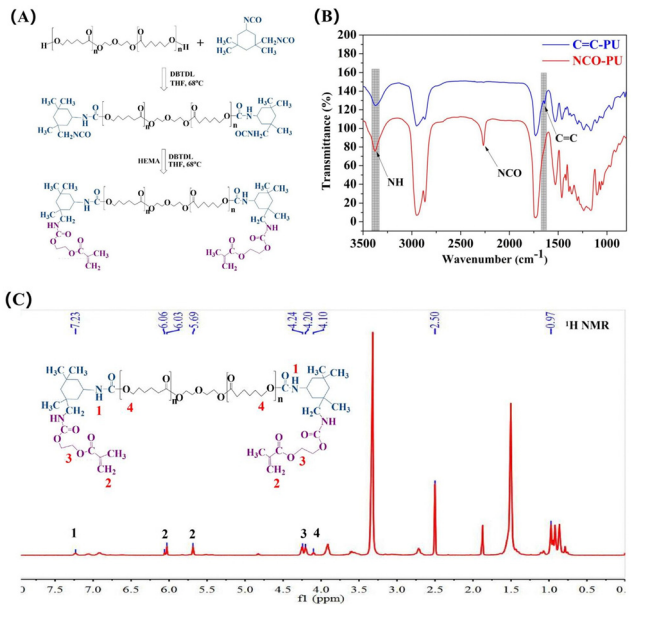

Fig. 1 Fabrication and characterization of photopolymerizable PU. (A) Synthetic routes of PU. (B) FT-IR spectra and (C) ^{1}H NMR spectra of PU.

terminated PU (photopolymerizable PU). Fig. 1B shows the FTIR spectra of the resulting prepolymers. For the NCO-terminated PU prepolymers obtained in the first step, the characteristic peak of the NCO group was observed at 2260 cm^{-1} and the characteristic signals of the –C═O ester stretching vibration was observed at 1725 cm^{-1}. The urethane bond (–NHCOO–) was observed at around 3340 cm^{-1}, which attributed to the reaction between the NCO group and OH group. Then, the C═C stretching vibration bond emerged at 1640 cm^{-1} after adding HEMA, and the NCO group disappeared. The ^1H NMR spectra also confirmed the successful synthesis of photopolymerizable PU (Fig. 1C). The peak at 4.10 ppm corresponded to the H of CH_2 from the PCL polyol and the peak at 7.11–7.21 ppm corresponded to the H of N–H from the main chain of IPDI. The characteristic peaks of –NH and –NH–CH_2– groups were both related to the PU prepolymers. After the reaction with HEMA, the PU prepolymer was functionalized with methacrylate groups. The distinct peaks in the double bond region (5.6–6.06 ppm) and a peak at 4.20–4.24 ppm were associated with the methylene bridges between the urethane groups and acrylate. Introducing methacrylate groups to PU was the essential step for subsequent crosslinking and network formation in 3D printing.

3.2 Characterization of NPP composites and scaffolds

3.2.1 Water contact angle and surface roughness. The wettability of NPP composites was examined using static water contact angles analysis. Fig. 2A and B show that the contact angles decreased with the increase of time. Generally, the components, the cross-linking density, the surface morphologies and the roughness of composites were closely related to the contact angle, while the measured static water contact angle values may fluctuate within a range. All the NPP composites have the largest water contact angle when the droplets touched the specimens at 0 s. The water infiltrated quickly at 20 s and 60 s due to the presence of POSS nanoparticles in the composites. It was reported that POSS could be interfused in the polymer *via* blending, copolymerization, or grafting and influence the surface chemistry (wettability), surface roughness and topography of the polymer matrix.[47] When compared with NPP-0%, POSS with methacrylate group (POSS MA0735) incorporation provided more cross-linking points, leading to a higher cross-linking density, thereby enhancing the hydrophobicity of the material surface. Hence, the water contact angle of NPP-5% was larger than those of NPP-0% and NPP-0% at 0 s. However, meanwhile, incorporating POSS prompted the formation of a porous structure and increased the roughness of the surface, which was also favorable for creating a hydrophilic surface.[39,48] The increased surface roughness in NPP-5% and NPP-10% was evidenced in comparison to NPP-0% by the AFM analysis (Fig. 2F). Overall, the NPP-5% and NPP-10% composites were more hydrophilic, which could promote cell adhesion and appropriate for cell proliferation.

3.2.2 Thermal characterization. DSC and TGA were used to evaluate the thermal properties of the NPP composites. Fig. 2C shows that the glass transition temperatures (T_g)

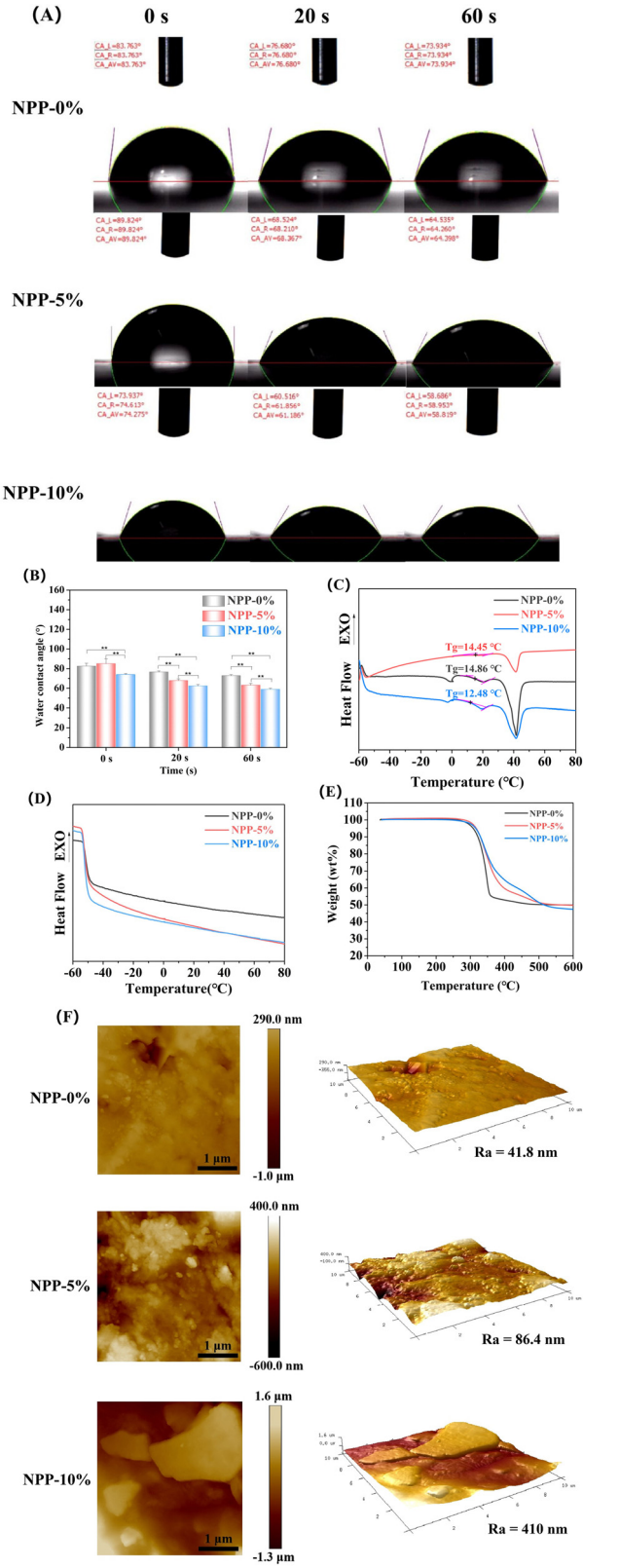

Fig. 2 Characterization of different NPP composites. (A and B) Water contact angle measurements. (C) DSC results of NPP-0%, NPP-5% and NPP-10% composites. (D) DSC results of NPP-0%, NPP-5% and NPP-10% composites after cross-linking. (E) TGA curves of NPP-0%, NPP-5% and NPP-10% composites with a temperature increase rate at 10 °C min^{-1}. (F) AFM 3D images of NPP-0%, NPP-5% and NPP-10% composites (**$p < 0.01$).

of the NPP composites were in the range of 12.49–14.86 °C. After cross-linking, as seen in Fig. 2D, no visible exothermic or endothermic peaks were observed in the same areas, indicating that the NPP composites were cured. According to the TGA thermograms (Fig. 2E), the degradation onset temperatures at 5 wt% loss ($T_{5\%}$) of NPP-0%, NPP-5%, and NPP-10% were 304.15, 314 and 311.38 °C, respectively. This indicated that the degree of thermal degradation was not significantly influenced by the POSS content. The thermal stabilities of PU and PU-containing composites depend on many factors, such as the fabrication conditions, reactants and additives.[37] Increasing the POSS loading from 0% to 10% progressively generated more cross-linking and network structures. Composites with a high cross-linking density generally have excellent thermal stability, partly because the diffusion of the matrix is restricted in a highly crosslinked polymer. However, the heterogeneous dispersion and agglomeration of POSS in the PU matrix also changed the decomposition diffusion pathways of PU and slightly affects its thermal stability. Therefore, the thermal degradation temperature of NPP-5% was the highest because of its high cross-linking density. In contrast, the thermal degradation temperature decreased slightly in NPP-10% due to heterogeneous dispersion and agglomeration. In general, all three NPP composites were thermally stable, and sufficient for the high temperature sterilization of the scaffold before clinical use.[36]

3.2.3 Rheology and printability. To achieve suitable rheological properties and shape reliability, a photocrosslinked composite material used for extrusion-based printing generally has shear thinning characteristics.[44] During extrusion, a decreased shear stress at a high shear rate reduced the viscosity of the composite to afford the optimal flow through the printer syringe. Then, the viscosity increased sharply once the material was deposited to maintain the structural integrity.[49] As illustrated in Fig. 3E, the viscosities of POSS-containing materials were lower than that of NPP-0%, possibly as a result of the longer polymer chain of PU than that of POSS. At the same extrusion pressure and/or speed, the strands deposited from the nozzle were wider in low viscosity groups (Fig. 3F and G). Both NPP groups showed the shear-thinning behavior in the shear rate range of 0.1–1000 s^{-1}, which was favorable for the printing process. Next, we evaluated the capability of NPP composites to be printed complicated 3D structures. After adjusting the printing parameters, a multi-layered scaffold in different shapes with a fiber diameter of ~400 μm was obtained, demonstrating a high printing resolution (Fig. 3A–D).

3.2.4 Mechanical properties. Mechanical properties are one of the most crucial clinical criteria for bone scaffolds.[44,50] An ideal bone scaffold should match host bone properties, provide an adequate support, and ensure appropriate load transfer during the regeneration of bone defects. In addition, toughness and elasticity are the other two indispensable requirements for scaffold materials to avoid sudden fractures after implantation.[44,50] Fig. 4 shows the mechanical properties of NPP scaffolds. The stress–strain curves (Fig. 4A and B)

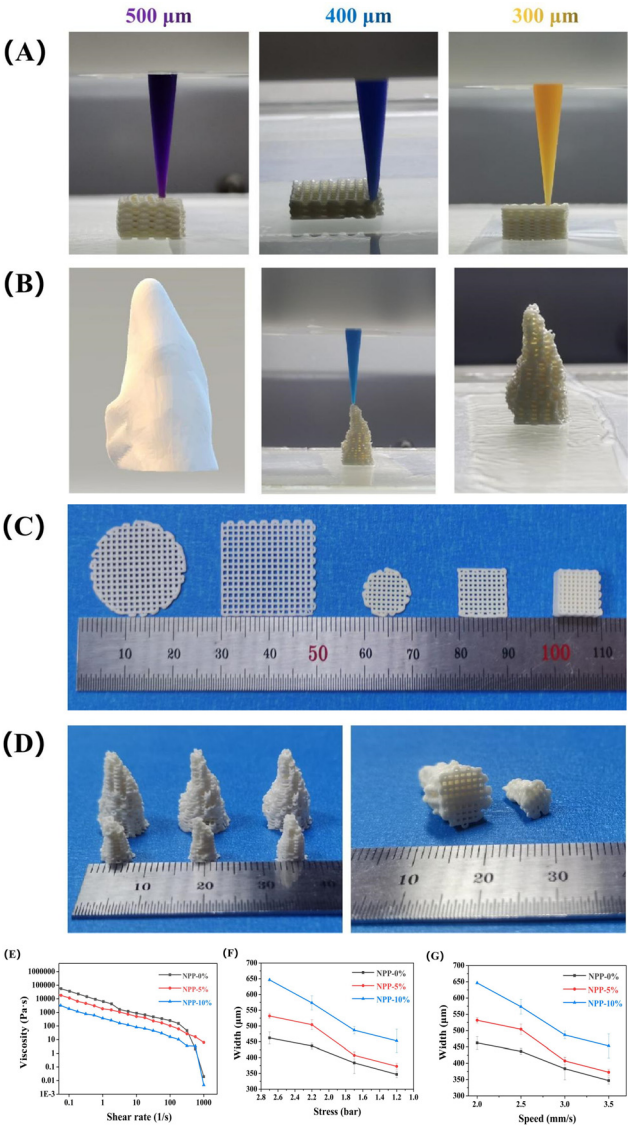

Fig. 3 Rheology and printability evaluation of NPP composites. (A–D) Images of multi-layered scaffolds in different shapes printed with NPP composites. (E) Viscosity *versus* shear rate profiles of different NPP composites. (F) Stress–width and (G) speed–width curves of the fiber diameter with different materials.

indicated that the mechanical properties of the scaffolds depended on the POSS content. In detail, the compressive moduli of NPP-5% and NPP-10% were significantly higher than that of NPP-0% (Fig. 4D) because the POSS moieties incorporated in the network strengthened the matrices. In addition, the photo-initiated polymerization of the methacrylate groups on the POSS and PU chains could lead to a higher cross-linked density of covalent networks. When the POSS content reached 10%, the compressive stress and modulus of the NPP scaffolds decreased (Fig. 4C and D). In this case, the POSS tended to agglomerate, leading to an uneven distribution within the scaffold and obstruction or auto-polymerization in the photo-crosslinking process. This trend was consistent with water contact angle measurements.

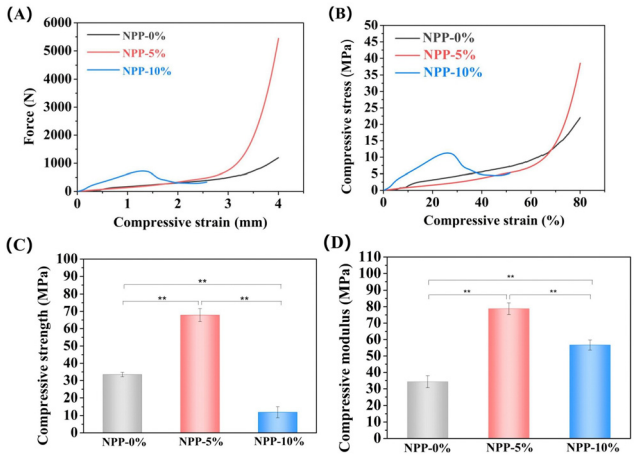

Fig. 4 Compressive properties of different NPP composite scaffolds. (A) Force–strain curve, (B) stress–strain curve, (C) compressive strength and (D) compressive modulus of the NPP-0%, NPP-5% and NPP-10% scaffolds in the compressive test (**$p < 0.01$).

3.3 Biomineralization *in vitro*

The production of an hydroxyapatite (HAP) layer confirms the capacity of a bone scaffold to create interfacial bonds with tissues around when in contact with physiological fluids, and the formation of apatite in SBF is related to the *in vivo* bone bioactivity.[51] Hence, the surface morphologies of NPP scaffolds after 7 days of immersion in SBF were characterized by SEM and EDS to evaluate apatite formation (Fig. 5). Compared to the scaffolds without SBF immersion (Fig. S1, ESI†), a large number of apatite crystalline aggregates were observed in all scaffolds (Fig. 5A). These apatites exhibited a plate-like morphology and formed a high-density 3D flowerlike structure, which was similar to the vertebrate long bones and tooth enamel. Furthermore, EDS analysis (Fig. 5B) showed evident Ca and P peaks in the NPP scaffolds after SBF immersion. The Ca/P ratios increased with the increasing POSS content. The Ca/P ratio of NPP-5% was in close proximity to the stoichiometric Ca/P ratio of pure HAP (Ca/P = 1.67). It has already been confirmed that nacre-containing composites have good apatite-forming bioactivity and can bond well to living bone tissues when implanted *in vivo*.[51] Meanwhile, previous studies have also demonstrated that silicon in POSS nanoparticles could bind to Ca^{2+} and induce HAP deposition on the material surface.[38] When POSS was incorporated in the composite, the increased Ca/P ratios indicated that the NPP scaffolds had better apatite-forming bioactivity.

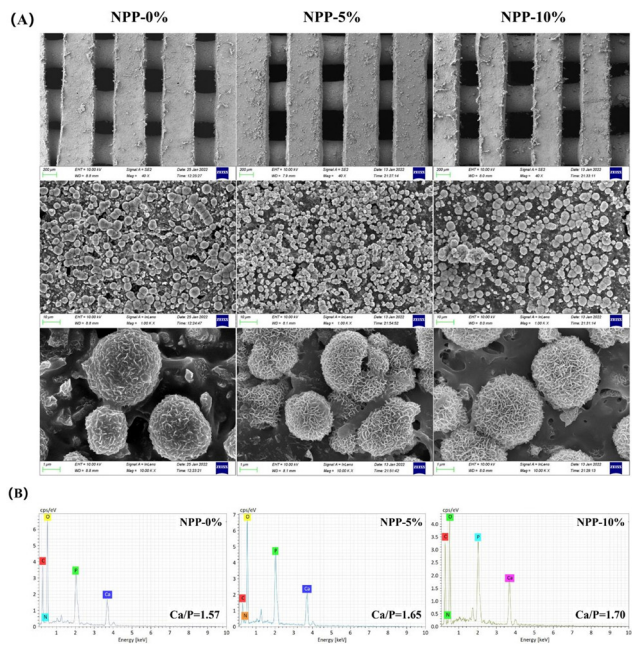

Fig. 5 (A) SEM images and (B) EDS analysis of the NPP-0%, NPP-5% and NPP-10% scaffolds after soaking in SBF for 7 days.

3.4 Cell proliferation and live/dead assay

Fig. 6 displays the cell compatibility and proliferative activity of MC3T3-E1 cells cultured in the NPP scaffolds for 1 and 3 days,

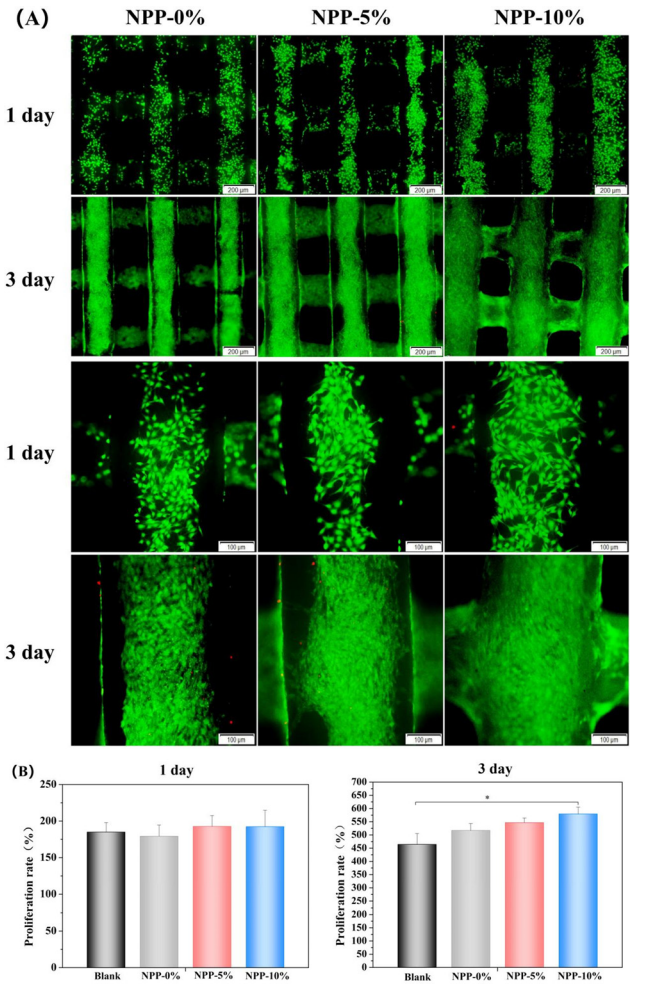

Fig. 6 Cytocompatibility of different NPP scaffolds by co-culturing with MC3T3-E1 cells for 1 and 3 days. (A) Live/Dead staining at 1 and 3 days; green fluorescence indicated viable cells and red fluorescence indicated dead cells. (B) Cell proliferation measured using the Alamar Blue assay (*$p < 0.05$).

wherein live and dead cells are indicated by green fluorescence and red fluorescence, respectively. After one day of culture, the cells adhere to the surface of scaffolds evenly. The cells on all the NPP scaffolds seemed to have elongated and polygonal morphology with a large cell area (Fig. 6A), indicating that the NPP scaffolds could boost the cell adhesion due to the satisfactory cytocompatibility of nacre,[24] PU[52] and POSS.[40] The proliferative activity on the three scaffolds was not obviously different on day 1, probably because the attachment of cells was in the early stages and the cells had just adhered to the wall and remained in the adaptation phase. After 3 days, live/dead staining showed that most cells remained alive, and proliferation differences gradually appeared ($P < 0.05$). These results are in accordance with the fluorescence results of the Alamar Blue assay (Fig. 6B). Notably, the NPP-10% scaffolds exhibited the most developed spindle-shaped morphology with the cells occupying the largest area compared to other groups. Introducing POSS could initiate the cellular response to form hydroxyapatite (HAP) so that the scaffolds were covered by a layer of HAP minerals. This would be the main reason for the enhanced cell adhesion and proliferation.[38] Moreover, we inferred that the cell proliferation was less likely to be influenced by the mechanical modulus of the scaffolds. Instead, the hydrophilicity of the material surface would be the dominate factor because it provided a suitable microenvironment for cell adhesion and proliferation. These results suggested that the three NPP scaffolds had no obvious toxic effects on the cells and exhibited satisfactory cytocompatibility, which was a fundamental requirement for the successful application of socket preservation materials.

3.5 Cell osteogenic differentiation

Furthermore, promoting cell adhesion and proliferation, an ideal scaffold for bone regeneration, should have beneficial properties to enhance the differentiation of cells and promote osteogenesis, which is regulated by the mechanical and chemical properties.[53,54] Following the synthesis and property screening, NPP-5% scaffolds were selected for the osteogenic differentiation evaluation because of their excellent mechanical properties, rheology, printability, and cell adhesion. To confirm the effect of POSS on osteogenesis, the NPP-0% scaffold was selected as a control. ALP staining and the osteogenesis-related gene expression of ALP were measured for 7 days to investigate the function of various scaffolds on the osteogenesis of MC3T3-E1 cells. ALP is an extremely important component of bone matrix vesicles and plays a vital role in the nascent stages of bone matrix mineralization, which is considered an early indicator of bone-specific markers.[44] Prior studies have demonstrated that nacre powder could promote the synthesis of the sialoprotein in jaw osteoblasts, and induce the expression of ALP genes.[26,55] In our study, the ALP-positive area was obviously larger in the NPP-5% groups than those in the other two groups for 7 days (Fig. 7A). The expression level of ALP genes further confirmed this significant difference. The genes were drastically upregulated in MC3T3-E1 cells in the NPP-5% scaffold groups, and there was no significant difference in the

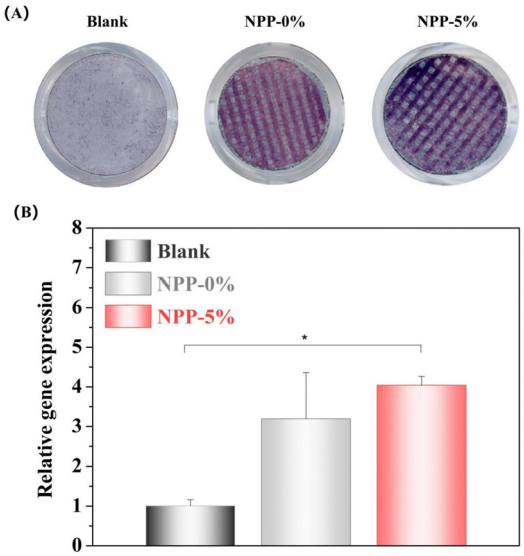

Fig. 7 *In vitro* evaluation of the osteogenic differentiation of MC3T3-E1 cells on different NPP scaffolds after 7 days of incubation. (A) Scanning images of ALP staining. (B) ALP gene expressions after culture with different NPP scaffolds for 7 days (*$p < 0.05$).

ALP expression level between the NPP-5% and NPP-0% groups (Fig. 7B). Then, alizarin red staining (ARS) was implemented to visualize the bone-like inorganic calcium deposits, which was the late osteogenic differentiation efficiency marker (Fig. S2, ESI†). Although the positive red-orange deposits were observed in all groups, the NPP-5% group showed significantly more deposits than the NPP-0% group. This phenomenon could be attributed to the synergy effect of the POSS supplementation and increased surface stiffness. In addition, incorporated nacre could gradually release Ca^{2+}, inducing the osteogenic differentiation of cells through the calcium/calmodulin signaling.[44,55,56]

3.6 Alveolar ridge preservation and *in vivo* osteogenesis

The *in vivo* biological evaluation using animal experiments is the key to developing materials for clinical applications. Fig. 8A shows the representative 3D reconstructed micro-CT images of the rat model's mandibular right first incisor sockets at weeks 3 and 6 after extraction. The soft tissue did not show any clinical signs of infection or wound dehiscence at the test or control sites, and the gingival tissue re-established its original color and fullness during the healing period (Fig. S3D and E, ESI†). The alveolar bone height and width in labial and lingual areas of all groups were reduced in a different scale after tooth extraction (Fig. 8B). The absorption rate of the NPP-5% scaffold group was less than those in the other two groups in both the labial or lingual plates ($P < 0.05$). In particular, the width losses in the labial plates of NPP-0% and NPP-5% scaffold groups were less significant than that of the control group (Fig. 8E, F, H and I). This was because the excellent mechanical strength of the NPP scaffold material could support the alveolar ridge in early stages and avoid its absorption and collapse.[46,57] In addition, previous *in vitro* experiments showed that the

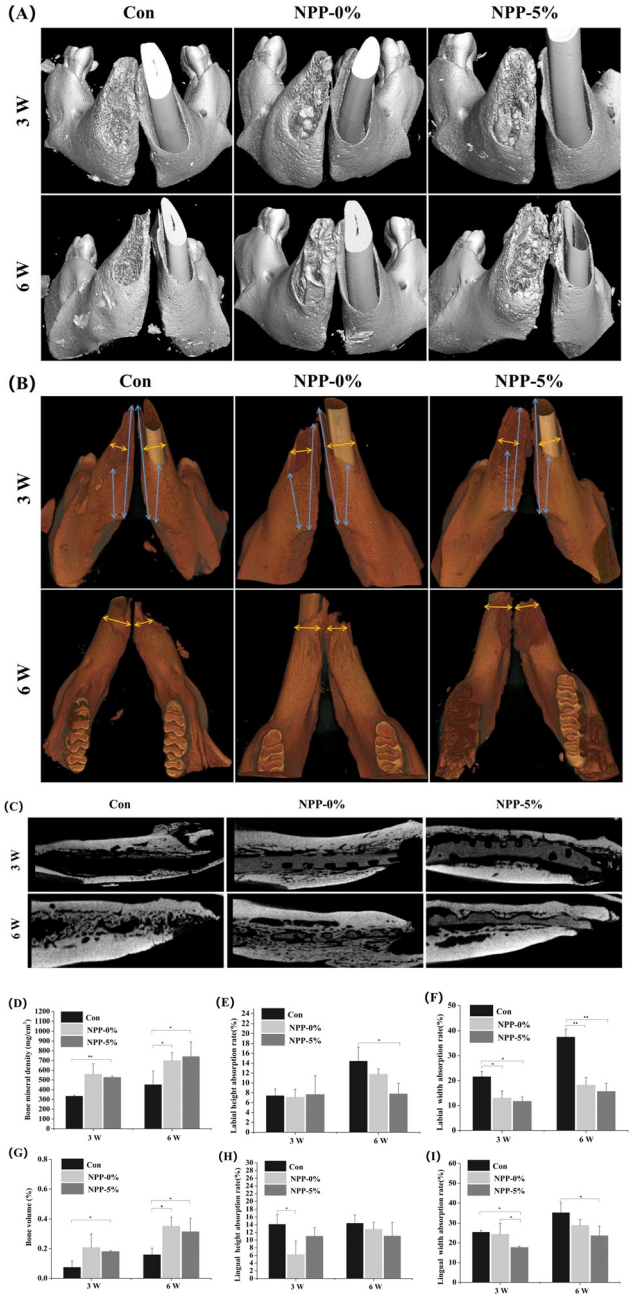

Fig. 8 Alveolar ridge preservation and *in vivo* osteogenesis. (A and B) Three-dimensional reconstruction images of the rat tooth extraction sockets filled with different NPP scaffolds or no scaffold (Con: control) after 3 and 6 weeks. (C) Analyses of the lateral sagittal section of the extraction, (D) bone mineral density (BMD), (E and F) absorption rates of the height and width in labial alveolar ridges, (G) bone volume ratio (BV/TV), and (H and I) absorption rates of the height and width in lingual alveolar ridges at weeks 3 and 6. The absorption rate (%) was calculated by the equation: $(1-(h1/h2))/100$, where $h1$ and $h2$ are the heights of the alveolar bone on the extracted and non-extracted sides, respectively ($*p < 0.05$, $**p < 0.01$).

activity of cathepsin *K* was specifically inhibited by some organic molecules in the nacre, decreasing the bone resorption activity and limiting osteoclastic bone resorption.[25] On the one hand, compared to the injectable *in situ* cured material or the nonporous solid plug material, 3D printed scaffolds had better efficacy in bone defect repair as the porous architecture allows new tissue infiltration.[44] On the other hand, their well-controlled geometry could match the individual socket shape and the alveolar bone defect shape. Therefore, NPP scaffolds showed a strong ability to reduce tooth extraction-induced alveolar bone resorption.

As expected, the NPP scaffold groups showed better new bone tissue accumulation, consistent with the aforementioned *in vitro* osteogenesis results, demonstrating that nacre and/or POSS could further increase the osteogenesis *in vivo*. As shown in Fig. 8C, in the NPP scaffold group, more new bone tissue was observed inside the extraction than that in the blank control group, in accordance with the bone mineral density (BMD) (Fig. 8D) and new bone volume ratio (BV/TV) (Fig. 8G). Interestingly, both the NPP-0% and NPP-5% scaffolds revealed higher BMD and BV/TV values than the blank control groups at week 6. The NPP-5% group had a higher BMD values but lower BV/TV values than NPP-0% group. This difference was not statistically significant and likely due to their different crosslinked density. The more crosslinked structure in NPP-5% led to a lower degradation, thus could not provide more space for the formation of the new bone. The higher BMD values in NPP-5% groups also confirmed that POSS could significantly enhance bone regeneration. Alveolar ridge preservation refers to ''any procedure undertaken at the time of, or following, an extraction that is designed to minimize the external resorption of the ridge and maximize bone formation within the socket''.[3] Similarly, the development of socket preservation materials presumably requires the combination of materials that inhibit bone resorption and induce the new bone formation. To the best of our knowledge, there have been no reports on the NPP scaffolds for socket preservation. Our study demonstrated that NPP scaffolds might effectively minimize the resorption of the alveolar ridge, showing great potential as a scaffold for site preservation after tooth extraction.

H&E staining was applied to evaluate the formation of new bone within the tooth extraction site after 3 weeks (Fig. 9A–F) and 6 weeks (Fig. 9G–L) post-NPP scaffold implantation. In all images, no significant inflammatory reaction was observed in either the control or the NPP scaffold group. After 3 weeks, the fibrous tissues predominated in the interior zone for all the three groups. No new bone tissues were formed in the center of the tooth extraction site in the control group. Meanwhile, only a small quantity of new bone formation was found in the edge area close to the hosting bone (Fig. 9A). In contrast, the NPP scaffold groups showed the obvious formation and mineralization of the new bone, and a certain number of new bone deposition was present along the surface of the scaffolds in the central region of the defect (Fig. 9C and E). After 6 weeks, the center of the tooth extraction site in the control group was full of fibrous tissues with some new bone tissues (Fig. 9G). The NPP-5% scaffold remained structurally integral, and the new bone tissues had grown into its holes (Fig. 9K). Meanwhile, the NPP-0% scaffold was slightly damaged with a thick fibrous tissue at the boundary (Fig. 9I). Compared with the NPP-0%

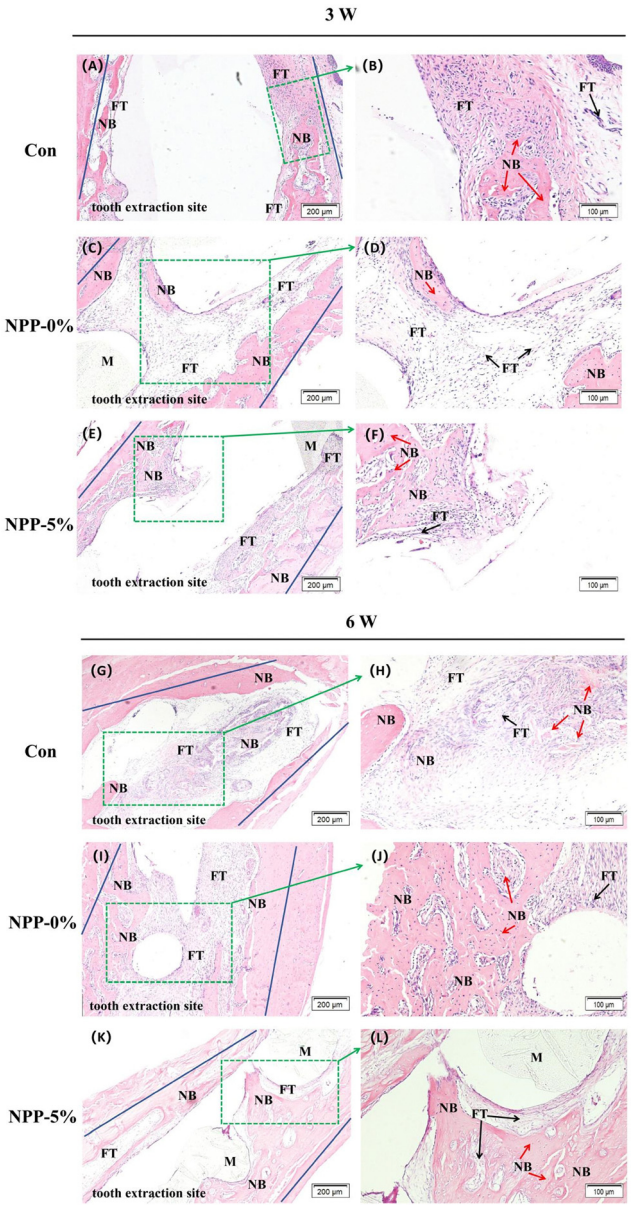

Fig. 9 H&E staining of bone regeneration in the tooth extraction sockets at weeks 3 and 6. Con group (A, B, G and H); NPP-0% group (C, D, I and J); NPP-5% group (E, F, K and L). The region in the green dotted box was magnified, and the image was shown along the green arrow. Red arrows: bone cells embedded in the bone matrix; black arrows: fibrous tissue layers. NB: new bone; FT: fibrous tissues; M: scaffold material.

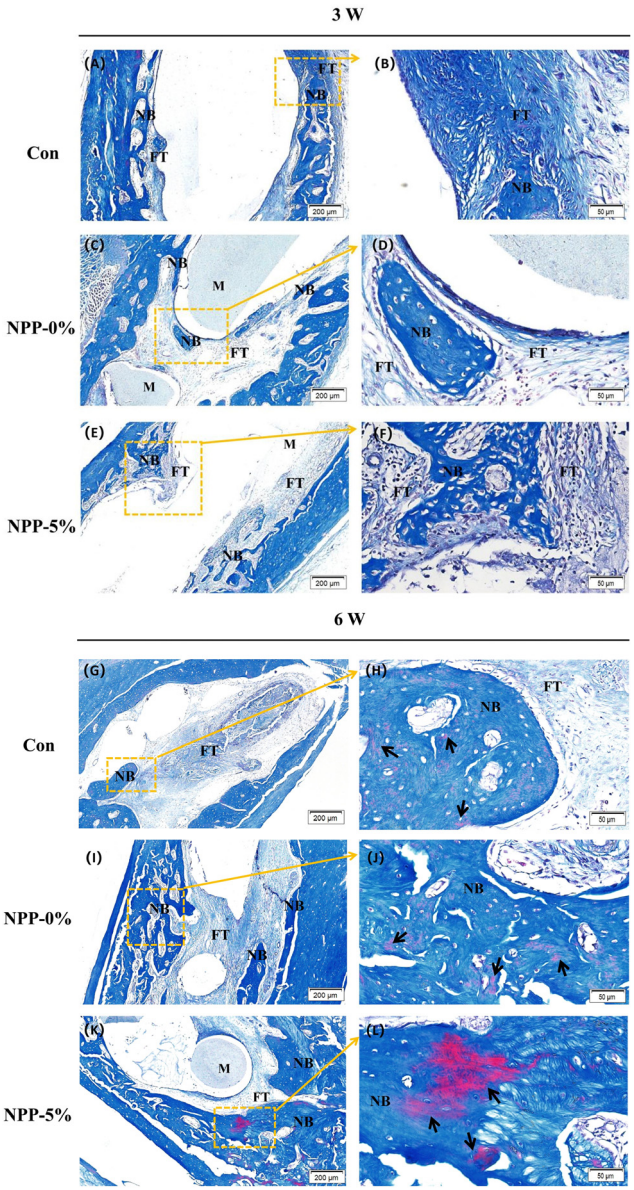

Fig. 10 Masson staining of bone regeneration in the tooth extraction sockets at weeks 3 and 6. Con group (A, B, G and H); NPP-0% group (C, D, I and J); NPP-5% group (E, F, K and L). The region in the yellow dotted box was magnified, and the image was shown along the yellow arrow. Black arrows: mature bone tissue. NB: new bone; FT: fibrous tissues; M: scaffold material.

scaffold group, the NPP-5% scaffold group showed numerous newly generated mature bone tissues instead of fibrous tissues or immature bone.

The Masson staining analysis (Fig. 10) was closely related to the degree of collagen maturation in the bone tissue (Fig. 10), and the trends were the same as those of H&E staining. The new and old bones could be distinguished by the coloration of the water-soluble dyes in the bone matrix.[38] When the bone tissue has matured, the color changes from blue to red. So, the blue area represents the new bone tissue or collagen, and the red area is the mature bone.[38] The bone tissue gradually matured in all three groups in a time-dependent manner; more new bone tissues were observed in the NPP scaffolds than in the control group at all time points. After 6 weeks, a good deal of mature collagen and regenerated bone tissue (blue area) grew into the scaffolds, and the NPP-5% scaffold group had a larger area of red stained (mature bone tissue) than the other groups. These results agree closely with the micro-CT analysis.

Finally, the histological examination of vital organs (liver, heart, spleen, and kidney) was performed after the implantation of scaffolds for 6 weeks by H&E staining to further evaluate the biocompatibility of the NPP scaffolds. As shown in Fig. 11, no noticeable inflammatory reaction or organ damage was

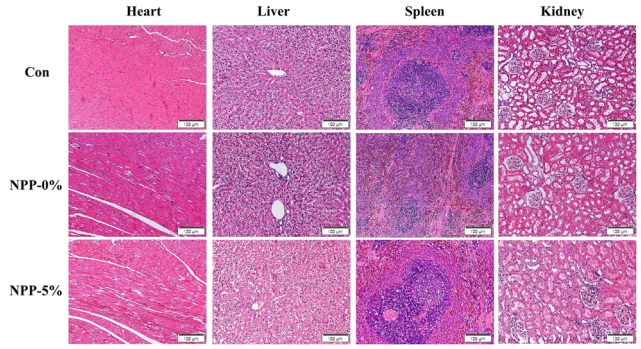

Fig. 11 Histological sections of the heart, liver, spleen and kidneys of the rats implanted with different NPP scaffolds or no scaffold (Con:control) at week 6.

observed in any group, further indicating that the NPP scaffolds had no toxicity *in vivo* and possessed good biocompatibility.

4. Conclusions

To reduce the resorption of alveolar ridges after tooth extraction, a novel 3D interconnected porous scaffold was successfully developed using an inorganic–organic composite ink consisting of PU, nacre, and POSS. These composite inks were desirable for extrusion-based 3D printing, as they exhibited remarkable shear-thinning behavior and could be photocrosslinked. In terms of mechanical properties, compared with NPP-0% scaffolds, the compressive stress and modulus of NPP-5% scaffolds were significantly improved, making the printed scaffolds suitable for load-bearing applications. Furthermore, both *in vitro* cell assays and *in vivo* studies demonstrated the excellent properties of biocompatibility and osteogenic potential of the printed NPP scaffolds. In summary, the photocrosslinked NPP scaffolds have excellent printability, mechanical properties, biocompatibility, and osteoinductive activity, showing great potential for alveolar ridge preservation.

Author contributions

H. Gong: conceptualization, methodology, investigation, software, data curation, formal analysis and writing – original draft; Y. Zhao: investigation and validation; W. Chen: software and formal analysis; Y. Wang and H. Zhao: methodology and software; J. Zhong: software; Q. Lan: validation; Y. Jiang: conceptualization and supervision; W. Huang: provided the laboratory resources and funding, and supervised the project.

Conflicts of interest

There are no conflicts to declare.

Acknowledgements

This work was financially supported by the National Natural Science Foundation of China (Grant no. 31972915), the Characteristic Innovation Projects of Ordinary Universities in Guangdong Province (Grant no. 2020KTSCX040), and the Guangdong Basic and Applied Basic Research Foundation (Grant no. 2020 B1515120001). The authors would like to acknowledge those who contributed to this article.

Notes and references

1 K. Jones, C. Williams, T. Yuan, A. M. Digeorge-Foushee, R. Chambers Wilson, T. Burton, N. Hamlin and L. Martinez, *J. Periodontol.*, 2022, **93**, 403–411.
2 J. B. Lee, S. Chu, H. Ben Amara, H. Y. Song, M. J. Son, J. Lee, H. Y. Kim, K. T. Koo and I. C. Rhyu, *J. Periodontol.*, 2021, **92**, 1564–1575.
3 L. Nie, H. Zhang, A. Ren, Y. Li, G. Fu, R. D. Cannon, P. Ji, X. Wu and S. Yang, *Dent. Mater.*, 2019, **35**, 1397–1407.
4 M. Okada, T. Matsuura, T. Akizuki, S. Hoshi, A. Shujaa Addin, S. Fukuba and Y. Izumi, *J. Periodontol.*, 2019, **90**, 1014–1022.
5 B. T. Goh, L. Y. Teh, D. B. P. Tan, Z. Zhang and S. H. Teoh, *Clin. Oral. Implants Res.*, 2015, **26**, 271–277.
6 N. MacBeth, A. Trullenque-Eriksson, N. Donos and N. Mardas, *Clin. Oral. Implants Res.*, 2017, **28**, 982–1004.
7 T. Yang, P. Xie, Z. Wu, Y. Liao, W. Chen, Z. Hao, Y. Wang, Z. Zhu and W. Teng, *Front. Bioeng. Biotechnol.*, 2020, **8**, 119.
8 N. Baldini, M. De Sanctis and M. Ferrari, *Dent. Mater.*, 2011, **27**, 61–70.
9 Z. Sheikh, C. Sima and M. Glogauer, *Materials*, 2015, **8**, 2953–2993.
10 M. Corrêa, L. R. Corrêa, A. Aragones and R. de Souza Magini, *Implant Dent.*, 2017, **26**, 832–840.
11 X. Wang, Y. Yu, C. Yang, C. Shao, K. Shi, L. Shang, F. Ye and Y. Zhao, *Adv. Funct. Mater.*, 2021, **31**, 2105190.
12 J.-Y. Shim, Y. Lee, J.-H. Lim, M.-U. Jin, J.-M. Lee, J.-Y. Suh and Y.-G. Kim, *Implant Dent.*, 2018, **27**, 623–629.
13 A. Scabbia and L. Trombelli, *J. Clin. Periodontol.*, 2004, **31**, 348–355.
14 L. Marinucci, S. Balloni, E. Becchetti, G. Bistoni, E. M. Calvi, E. Lumare, F. Ederli and P. Locci, *Ann. Biomed. Eng.*, 2010, **38**, 640–648.
15 M. G. Araújo, J. C. C. da Silva, A. F. de Mendonça and J. Lindhe, *Clin. Oral. Implants Res.*, 2015, **26**, 407–412.
16 N. Broggini, D. D. Bosshardt, S. S. Jensen, M. M. Bornstein, C. C. Wang and D. Buser, *J. Biomed. Mater. Res., Part B*, 2015, **103**, 1478–1487.
17 R. E. Jung, A. Philipp, B. M. Annen, L. Signorelli, D. S. Thoma, C. H. Hämmerle, T. Attin and P. Schmidlin, *J. Clin. Periodontol.*, 2013, **40**, 90–98.
18 H. Shao, A. Liu, X. Ke, M. Sun, Y. He, X. Yang, J. Fu, L. Zhang, G. Yang and Y. Liu, *J. Mater. Chem. B*, 2017, **5**, 2941–2951.
19 L. Zhong, J. Chen, Z. Ma, H. Feng, S. Chen, H. Cai, Y. Xue, X. Pei, J. Wang and Q. Wan, *Nanoscale*, 2020, **12**, 24437–24449.
20 D. W. Hutmacher, *Biomaterials*, 2000, **21**, 2529–2543.

21 M. Zhang, R. Lin, X. Wang, J. Xue, C. Deng, C. Feng, H. Zhuang, J. Ma, C. Qin, L. Wan, L. Wan and J. Chang, *Sci. Adv.*, 2020, **6**, eaaz6725.
22 M. Li, P. Song, W. Wang, Y. Xu, J. Li, L. Wu, X. Gui, Z. Zeng, Z. Zhou, M. Liu, Q. Kong, Y. Fan, X. Zhang, C. Zhou and L. Liu, *J. Mater. Chem. B*, 2022, **10**, 4172–4188.
23 Q. Huang, Y. Liu, Z. Ouyang and Q. Feng, *Bioact. Mater.*, 2020, **5**, 980–989.
24 E. M. Gerhard, W. Wang, C. Li, J. Guo, I. T. Ozbolat, K. M. Rahn, A. D. Armstrong, J. Xia, G. Qian and J. Yang, *Acta Biomater.*, 2017, **54**, 21–34.
25 H. Kim, K. Lee, C.-Y. Ko, H.-S. Kim, H.-I. Shin, T. Kim, S. H. Lee and D. Jeong, *Biomaterials*, 2012, **33**, 7489–7496.
26 J. Pei, Y. Wang, X. Zou, H. Ruan, C. Tang, J. Liao, G. Si and P. Sun, *Front. Bioeng. Biotechnol.*, 2021, **9**, 292.
27 H. Liao, C. Brandsten, C. Lundmark, T. Wurtz and J. Li, *J. Mater. Sci.: Mater. Med.*, 1997, **8**, 823–827.
28 S. Berland, O. Delattre, S. Borzeix, Y. Catonné and E. Lopez, *Biomaterials*, 2005, **26**, 2767–2773.
29 M. Lamghari, S. Berland, A. Laurent, H. Huet and E. Lopez, *Biomaterials*, 2001, **22**, 555–562.
30 G. Atlan, N. Balmain, S. Berland, B. Vidal and É. Lopez, *C. R. Acad. Sci., Ser. III*, 1997, **320**, 253–258.
31 Y. Liu, Q. Huang and Q. Feng, *Biomed. Mater.*, 2013, **8**, 065001.
32 B. Naureen, A. S. M. A. Haseeb, W. J. Basirun and F. Muhamad, *Mater. Sci. Eng., C*, 2021, **118**, 111228.
33 F.-Y. Hsieh, H.-H. Lin and S.-H. Hsu, *Biomaterials*, 2015, **71**, 48–57.
34 K. C. Hung, C. S. Tseng and S. H. Hsu, *Adv. Healthcare Mater.*, 2014, **3**, 1578–1587.
35 M. W. Laschke, A. Strohe, M. D. Menger, M. Alini and D. Eglin, *Acta Biomater.*, 2010, **6**, 2020–2027.
36 A. Farzan, S. Borandeh, N. Z. Ezazi, S. Lipponen, H. A. Santos and J. Seppälä, *Eur. Polym. J.*, 2020, **139**, 109988.
37 H. Gong, X. Guo, D. Cao, P. Gao, D. Feng, X. Zhang, Z. Shi, Y. Zhang, S. Zhu and Z. Cui, *J. Mater. Chem. B*, 2019, **7**, 744–754.
38 X. Zhang, Y. He, P. Huang, G. Jiang, M. Zhang, F. Yu, W. Zhang, G. Fu, Y. Wang and W. Li, *Composites, Part B*, 2020, **197**, 108183.
39 M. Chen, Y. Zhang, W. Zhang and J. Li, *ACS Appl. Mater. Interfaces*, 2020, **12**, 22410–22425.
40 S. Liu, R. Guo, C. Li, C. Lu, G. Yang, F. Wang, J. Nie, C. Ma and M. Gao, *Eur. Polym. J.*, 2021, **143**, 110180.
41 S. Tamburaci, C. Kimna and F. Tihminlioglu, *Mater. Sci. Eng., C*, 2019, **100**, 196–208.
42 M. Rousseau, L. Pereira-Mouriès, M.-J. Almeida, C. Milet and E. Lopez, *Comp. Biochem. Physiol., Part B: Biochem. Mol. Biol.*, 2003, **135**, 1–7.
43 C. Wu, Y. Luo, G. Cuniberti, Y. Xiao and M. Gelinsky, *Acta Biomater.*, 2011, **7**, 2644–2650.
44 Y. Yang, Q. Zhang, T. Xu, H. Zhang, M. Zhang, L. Lu, Y. Hao, J. H. Fuh and X. Zhao, *Biomaterials*, 2020, **263**, 120378.
45 S. Chen, L. Zhu, W. Wen, L. Lu, C. Zhou and B. Luo, *ACS Biomater. Sci. Eng.*, 2019, **5**, 2506–2518.
46 Y. Pan, Y. Zhao, R. Kuang, H. Liu, D. Sun, T. Mao, K. Jiang, X. Yang, N. Watanabe and K. H. Mayo, *Mater. Sci. Eng., C*, 2020, **116**, 111158.
47 S. Tamburaci and F. Tihminlioglu, *Int. J. Biol. Macromol.*, 2020, **142**, 643–657.
48 X. Li, P. Xu, Y. Cheng, W. Zhang, B. Zheng and Q. Wang, *Mater. Sci. Eng., C*, 2020, **111**, 110749.
49 J. Malda, J. Visser, F. P. Melchels, T. Jüngst, W. E. Hennink, W. J. A. Dhert, J. Groll and D. W. Hutmacher, *Adv. Mater.*, 2013, **25**, 5011–5028.
50 S. Bose, M. Roy and A. Bandyopadhyay, *Trends Biotechnol.*, 2012, **30**, 546–554.
51 X. Zhang, X. Du, D. Li, R. Ao, B. Yu and B. Yu, *J. Biomater. Sci., Polym. Ed.*, 2018, **29**, 1686–1700.
52 P. Szczepańczyk, M. Szlachta, N. Złocista-Szewczyk, J. Chłopek and K. Pielichowska, *Polymers*, 2021, **13**, 946.
53 M. Chen, Y. Zhang, Q. Xie, W. Zhang, X. Pan, P. Gu, H. Zhou, Y. Gao, A. Walther and X. Fan, *ACS Biomater. Sci. Eng.*, 2019, **5**, 4612–4623.
54 J. H. Wen, L. G. Vincent, A. Fuhrmann, Y. S. Choi, K. C. Hribar, H. Taylor-Weiner, S. Chen and A. J. Engler, *Nat. Mater.*, 2014, **13**, 979–987.
55 X. J. Loh, D. J. Young, H. Guo, L. Tang, Y. Wu, G. Zhang, C. Tang and H. Ruan, *Materials*, 2021, **14**, 2797.
56 Y. C. Chai, A. Carlier, J. Bolander, S. J. Roberts, L. Geris, J. Schrooten, H. Van Oosterwyck and F. P. Luyten, *Acta Biomater.*, 2012, **8**, 3876–3887.
57 G. Chen, C. Dong, L. Yang and Y. Lv, *ACS Appl. Mater. Interfaces*, 2015, **7**, 15790–15802.